INL/EXT-06-12011

Fatigue Testing of Metallurgically Bonded EBR-II Superheater Tubes

Terry C. Totemeier

December 2006

The INL is a U.S. Department of Energy National Laboratory
operated by Battelle Energy Alliance

INL/EXT-06-12011

Fatigue Testing of Metallurgically Bonded EBR-II Superheater Tubes

Terry C. Totemeier

December 2006

Idaho National Laboratory
Idaho Falls, Idaho 83415

Prepared for the
Japan Atomic Energy Agency
Under Work for Others Agreement No. 85Q40
Under DOE Idaho Operations Office
Contract DE-AC07-05ID14517

ABSTRACT

Fatigue crack growth tests were performed on 2¼Cr-1Mo steel specimens machined from ex-service Experimental Breeder Reactor – II (EBR-II) superheater duplex tubes. The tubes had been metallurgically bonded with a 100 μm thick Ni interlayer; the specimens incorporated this bond layer. Tests were performed at room temperature in air and at 400°C in air and humid Ar; cracks were grown at varied levels of constant ΔK. Crack growth tests at a range of ΔK were also performed on specimens machined from the shell of the superheater. In all conditions the presence of the Ni interlayer was found to result in a net retardation of growth as the crack passed through the interlayer. The mechanism of retardation was identified as a disruption of crack planarity and uniformity after passing through the porous interlayer. Full crack arrest was only observed in a single test performed at near-threshold ΔK level (12 MPa√m) at 400°C. In this case the crack tip was blunted by oxidation of the base steel at the steel-interlayer interface.

CONTENTS

FIGURES

TABLES

Fatigue Testing of Metallurgically-Bonded EBR-II Superheater Tubes

1. Introduction

Fatigue crack growth (FCG) tests were performed on 2¼Cr–1Mo steel specimens machined from ex-service EBR-II superheater duplex tubes. The tubes were metallurgically bonded with a 100 µm thick Ni interlayer; the specimens incorporated the bond layer. The purpose of the testing was to evaluate the ability of the bond layer to retard or arrest cracks growing under cyclic loading conditions, supplementing previous impact testing of similar tube specimens that had confirmed the crack-arresting ability of the bond layer in dynamic, monotonic loading conditions (impact tests). FCG tests were also performed on 2¼Cr–1Mo steel specimens machined from the shell of the same superheater. The shell material did not contain a metallurgical bond; the results of these fatigue tests were used for comparison with bonded material and to assess the effect of thermal exposure during service on the fatigue properties of 2¼Cr–1Mo steel. A thorough suite of initial tests was performed in air at room temperature; a more limited set of tests at 400°C in air and humid Ar were subsequently performed. This report presents results from all tests performed to date.

2. Material and Test Procedures

Rectangular bend specimens were machined from sections of metallurgically-bonded 2¼Cr–1Mo steel tubes that had been cut from EBR-II superheater SU-710. Tube sections were removed from the upper and lower regions of the superheater, representing two different heat flux and thermal exposure conditions. Material from the lower region was exposed to an average temperature of 453°C with a 30°C temperature gradient (lower heat flux); material from the upper region was exposed to an average temperature of 366°C and a 124°C temperature gradient (higher heat flux). The dimensions of the bend specimens were $53.3 \times 3.8 \times 3.8$ mm^3, identical to the miniature Charpy V-notch impact specimens tested previously (Figure 1). Starter notches for FCG testing were cut so that the crack would grow in the radial direction in a plane normal to the axial direction of the original tube, thereby growing through the metallurgical bond layer in the center of the specimen. Specimens were notched so that crack growth occurred from both from the inside and outside of the tube. Notches were cut to a depth of 0.9 mm, initially with a jewelers' saw (0.5 mm width), and subsequently by electro-discharge machining (EDM) with a 0.5 mm wire.

Similar specimens were machined from the 2¼Cr–1Mo steel shell material, which had been exposed to a temperature of 485°C. Some shell specimens had a greater thickness (7.7 mm) to facilitate FCG testing under constant load range conditions. In this case starter notches 1.9 mm deep were cut (Figure 1). All tests at 400°C (both shell and bonded tube) were performed on the smaller specimens with $W = 3.8$ mm.

FCG tests were performed in 3-point bending on an Instron 8501 servo-hydraulic test machine. The requirements of ASTM test standard E 647-00 were followed to the extent possible given the small specimen sizes. A small servo valve and a 5 kN load cell were used to accurately generate and measure the low forces (~ 50-300 N) needed for testing the small specimens. For tests at 400°C the specimens and loading platens were heated in a box-type resistance furnace; the platens and loading rods were machined from a high-strength nickel alloy and stainless steel, respectively. Alumina rod was used for loading pins to electrically insulate the specimen (Figure 2). A type K thermocouple was spot-welded to the specimen to monitor temperature.

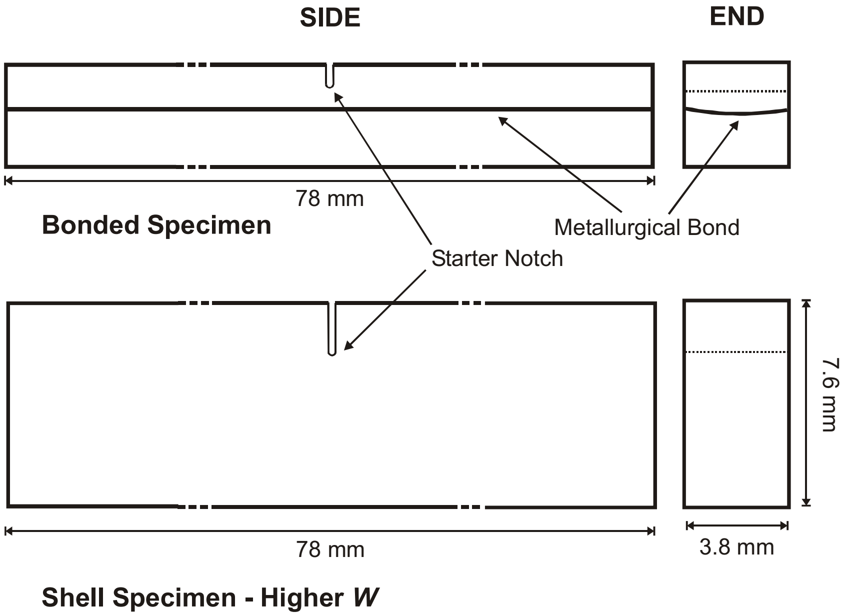

Figure 1. Schematic drawings of fatigue specimens

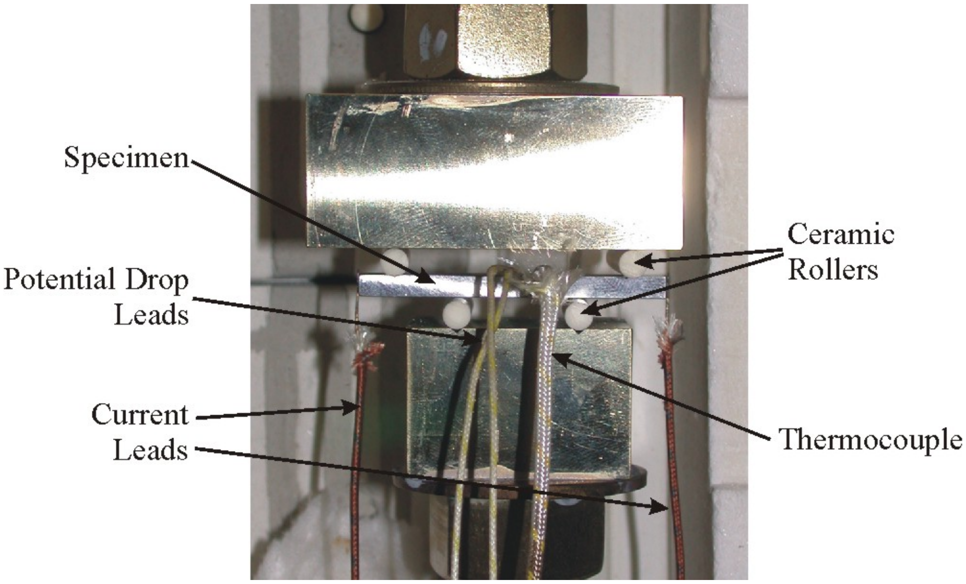

Figure 2. Set-up for fatigue crack growth tests at 400°C.

For some tests at 400°C a humid Ar atmosphere was created in the furnace as a crude simulation of a steam environment by flowing ultra-high-purity Ar through a bubbler containing distilled water at room temperature. The humidified Ar was then piped into the furnace via a stainless steel tube whose outlet was adjacent to the specimen. The interior of the box furnace was nominally sealed by stuffing gaps with alumina fiber insulation. Ar was continually flowed into the furnace during testing at a low flow rate (~ 100-500 ml/min, not measured).

Room-temperature FCG tests were performed in air with a sinusoidal waveform at a nominal cyclic frequency of 20-30 Hz. The frequency was lowered (to a minimum of 1 Hz) during conditions of rapid crack growth for better control. An R ratio ($= K_{\min}/K_{\max}$) of 0.1 was used for all tests except for one test where an R ratio of 0.45 was used to minimize crack closure effects. A sinusoidal waveform and R ratio of 0.1 were also used in tests at 400°C. Crack initiation was performed at 20 Hz; cracks were grown at this frequency to 1.15 mm length (0.3 a/W). At this point the frequency was lowered to 1 Hz and all subsequent loading occurred at this frequency, which roughly corresponds to the frequency thermal loading caused by departure from nucleate boiling (DNB) events.

Tests on bonded specimens were conducted at a pre-determined, constant level of stress intensity parameter range (ΔK). Three levels of ΔK were used, corresponding to the near-threshold (10-12 MPa√m), Paris law (15 MPa√m), and accelerating crack growth (20 MPa√m) regimes. The levels were selected based on results from the non-bonded shell material. Cracks were initiated from the notch at 14-15 MPa√m; for tests to be performed at a lower stress intensity range (i.e., near-threshold), the stress intensity was lowered to the test level after a very small (20 μm) increment of crack growth.

Room-temperature tests on unbonded shell material were conducted at a constant load range; ΔK increased as the crack grew allowing crack growth rates to be determined over a broad range of ΔK in a single test. Elevated temperature tests on shell material were conducted at a series of constant ΔK levels. The crack was grown at each ΔK level for a period sufficient to establish a measurable crack growth rate for that ΔK.

Crack lengths were measured during testing by the direct-current potential drop (DCPD) method. Current leads were attached to each end of the specimen; potential drop (PD) leads were spot welded to the specimen as shown in Figure 3. For room temperature tests the leads were nominally pure Fe; at elevated temperature Ni-Al alloy wire (Alumel thermocouple wire) was used to prevent oxidation of the leads. Two sets of leads were used in initial tests to detect possible asymmetric crack growth (left), a single set of leads were used in later tests (right), after the crack fronts had been shown to grow straight across the thickness of the specimen. A current of 10 A was used for room-temperature tests which resulted in a reference potential drop of approximately 500 μV. At 400°C a current of 5 A was used, also generating of reference potential drop of approximately 500 μV. A Tektronics TM506A current supply and a computer-based PD data acquisition system were used. PD readings were converted to normalized crack lengths (a/W, where a is the crack length and W the specimen width) using Johnson's equation as given in ASTM E 647-00. Load ranges were adjusted as the crack grew so that the ΔK level was maintained within ±0.2 MPa√m. Cracks were typically grown to a normalized length of 0.65-0.70. The specimens were then broken after cooling in liquid N_2 to clearly demark the final fatigue crack position.

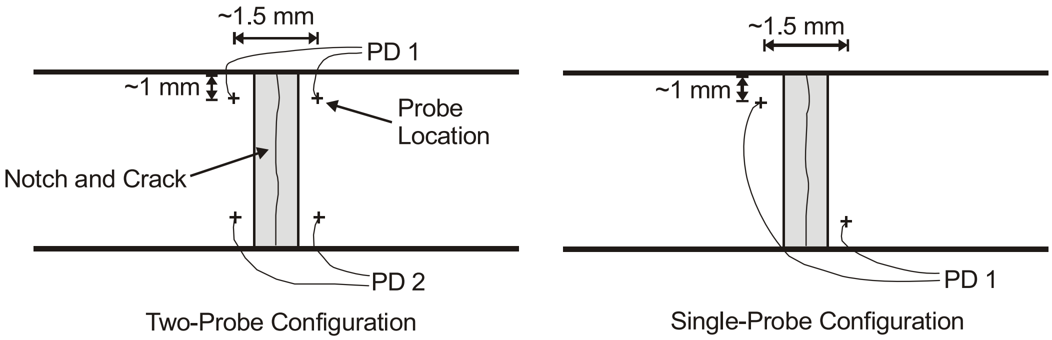

Figure 3. Potential drop lead configurations (schematic top view of specimen).

Due to the difficulty in precisely defining the probe spacing input to Johnson's equation (because of the relative magnitudes of specimen width, probe spacing, and probe wire diameter), the crack lengths used to calculate required load levels during the test were only approximate (~10% error). In some early tests the desired and actual ΔK levels significantly differed due to this approximation.

After testing, the final PD reading and the physically-measured final crack length were used to determine the effective probe spacing input to Johnson's equation, which was then used to calculate accurate crack lengths for all other PD readings. These crack lengths and measured load ranges were used to calculate actual ΔK levels applied to the specimen. Test data for the bonded specimens were plotted as crack length and ΔK versus number of cycles. Crack growth rates in different regions of the specimens were calculated from the a versus N data. Fatigue crack growth data from shell material was plotted as $\mathrm{d}a/\mathrm{d}N$ versus ΔK curves as described in ASTM E 647-00.

Post-test fractography was performed on selected specimens using stereo light microscopy at low magnifications and scanning electron microscopy at higher magnifications. Metallographic cross-sections of a specimen in which crack arrest occurred were prepared and examined.

3. Results

3.1 Shell Material

The results of tests on four different specimens of the non-bonded superheater shell material at room temperature are shown in Figure 4. The crack growth rates show a classical dependence on ΔK, with a fatigue threshold of approximately 10 MPa√m, Paris law behavior for ΔK between 11.5 and 25 MPa√m, and rates accelerating into stage III behavior above 25 MPa√m. Applying a power law fit to data in the Paris regime yields the following:

$$\mathrm{d}a/\mathrm{d}N = 1.3\times10^{-10}\,(\Delta K)^{4.5}$$

These crack growth rates are essentially identical to those reported in the CINDAS Structural Alloys Handbook (1996 edition) for 2¼Cr–1Mo steel in the same condition, so no significant change in room temperature fatigue crack growth resistance has occurred as a result of the long-term thermal exposure.

Crack growth rates in shell material at 400°C at 20 Hz in air and 1 Hz in humid Ar are compared with room-temperature data in Figure 5. Rates in the Paris regime are similar for the different temperatures and environments. Threshold values at 400°C, however, are higher than at room temperature, likely due to oxidation-induced crack closure effects. There are no significant differences between the air and humid Ar environments.

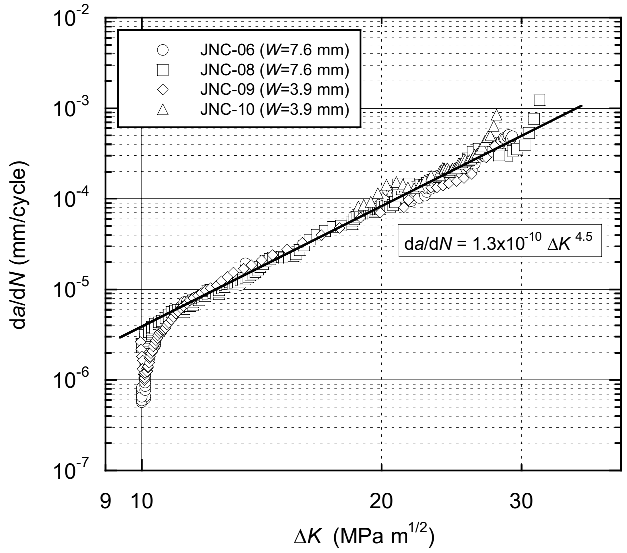

Figure 4. Room-temperature fatigue crack growth rates for superheater shell material.

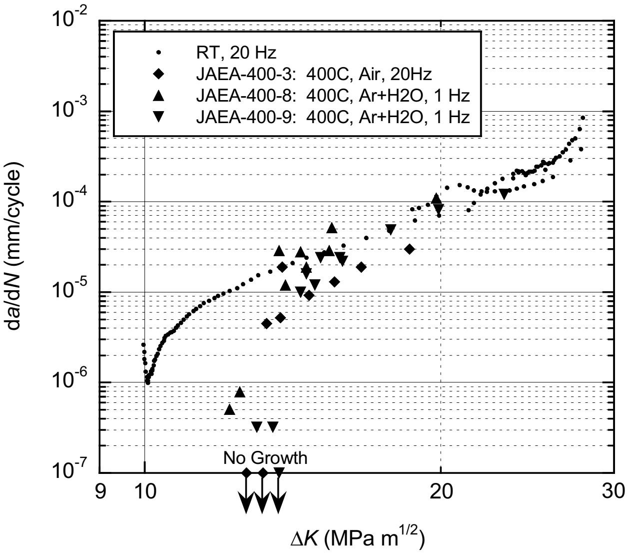

Figure 5. Comparison of shell crack growth rates at room temperature and 400°C.

3.2 Bonded Tube Material

3.2.1 Fatigue Crack Growth Rates – Room Temperature

The behavior of all specimens was similar; Figure 6 shows a typical test which was conducted at 14.5 MPa√m with the crack growing from inside to outside (specimen JNC-22). Normalized crack length is plotted as a function of cycles. The location of the metallurgical bond (determined from the fracture surface) is superimposed on the plot. The growth rate gradually accelerates as the crack grows away from the notch, reaching a constant rate of 2.2×10^{-5} mm/cycle prior to entering the bonded layer. The growth rate further accelerates just prior to and in the bond layer, achieving a maximum rate of 5.2×10^{-5} mm/cycle. The growth rate is markedly retarded for distance of 0.5 mm after the bond layer, growing at a rate of 8.9×10^{-6} mm/cycle. Near the end of the test the growth rate re-accelerates to a rate identical to that measured before the bond was entered, and grows at this linear rate until the test is terminated. The net retardation in crack growth in terms of number of cycles is equal to the X-axis offset of the two baseline curves, in this case about 20,000 cycles.

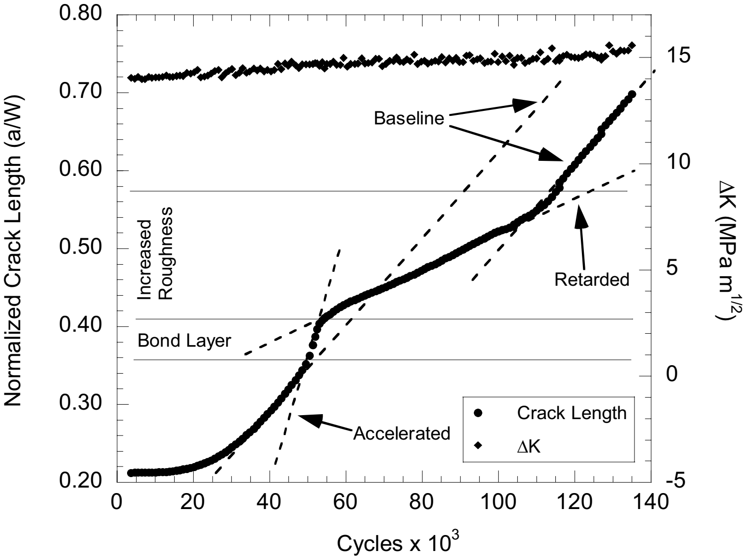

Figure 6. Normalized crack length versus cycles for test JNC-22: upper tube section, crack growing from inside to outside, nominal ΔK = 15 MPa√m.

Table 1 summarizes conditions for all tests on bonded tube specimens at room temperature and lists the growth rates measured in the different regions of each specimen: the baseline rate prior to the crack entering the bond; the accelerated rate observed just before and in the bond layer; the retarded rate after the bond; and finally the re-accelerated rate. Not all cracks were grown to sufficiently long lengths to measure the re-accelerated rate. In some of the first tests the ΔK computed from corrected cracks lengths after the test differed from the intended constant ΔK level. In these cases the actual ΔK level corresponding to the applicable region is given beneath the growth rate. A test on shell material at constant ΔK conditions was run to confirm that a constant rate would indeed be observed without the bond present; the *a*/*W* versus *N* curve for this specimen is shown in Figure 7.

Example plots for other conditions (i.e., low ΔK, high ΔK, and material from the lower tube section) are shown in Figures 8-10, illustrating the similarity of curves. The baseline rates did not vary with superheater location or crack growth direction and in all cases matched the rates obtained on shell material. The amount of acceleration and retardation due to the bond layer varied from test to test but was roughly a factor of 1.5 to 3 for acceleration (accelerated rate divided by baseline rate) and 2 to 4 for retardation (post-bond retarded rate divided by baseline rate). The accelerated rate in the bond layer increased with Δ*K*, varying from 1×10^{-5} mm/cycle at 12 MPa√m to 4×10^{-4} mm/cycle at 20 MPa√m. Exceptional behavior was observed for JNC-11, a test conducted near the threshold Δ*K* level. For this test the retarded rate was nearly an order of magnitude lower than the baseline rate.

Test JNC-24 was conducted at a higher *R* ratio (0.45) to observe the effect of crack closure on the acceleration and retardation behavior. The term crack closure refers to a reduction in crack growth rates due to the contact of crack wake surfaces at a load greater than the minimum load level of the fatigue cycle. Closure effects are lessened by increasing the minimum load, i.e., by testing at a higher *R* ratio. In this test *R* was limited to 0.45 by the need to keep K_{max} less than 25 MPa√m and keep Δ*K* greater than 12 MPa√m for comparison with previous tests. With respect to the baseline $R = 0.1$, crack growth rates were accelerated in all regions of the specimen, as expected, but the factors of acceleration and retardation were similar to previous tests. The lack of change in acceleration and retardation factors due to the bond indicates that closure effects on the processes accelerating and retarding crack growth in and after the bond are minimal.

3.2.2 Fatigue Crack Growth Rates – 400°C

The crack growth behavior observed in air and humid Ar at 400°C was essentially identical to that at room temperature. Cracks accelerated entering the bond region, were retarded exiting the bond region, and re-accelerated after the bond region, as shown in Figure 11 for a test performed in humid Ar. The magnitudes of acceleration and deceleration were similar to those at room temperature. One exception was the test conducted in air at 12 MPa√m (JAEA-400-6), in which a full crack arrest occurred, as shown in Figure 12. Test JAEA-400-11 was also conducted at a relatively low Δ*K* level (14.5 MPa√m), but in this case an order of magnitude growth rate reduction occurred instead of complete crack arrest. Also apparent in Figures 11 and 12 is an increase in crack growth rate for 1 Hz cycling compared to 20 Hz. Similar increased were observed in all tests at 400°C.

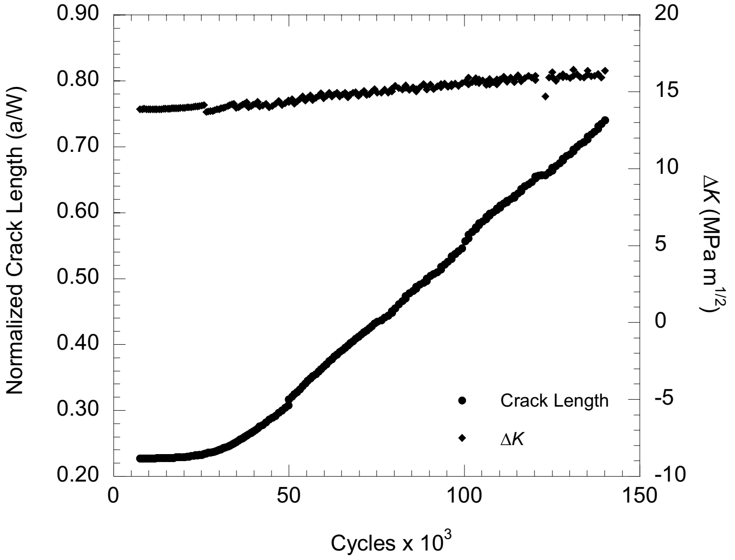

Figure 7. Normalized crack length versus cycles for test JNC-15: non-bonded shell material, nominal Δ*K* = 15 MPa√m.

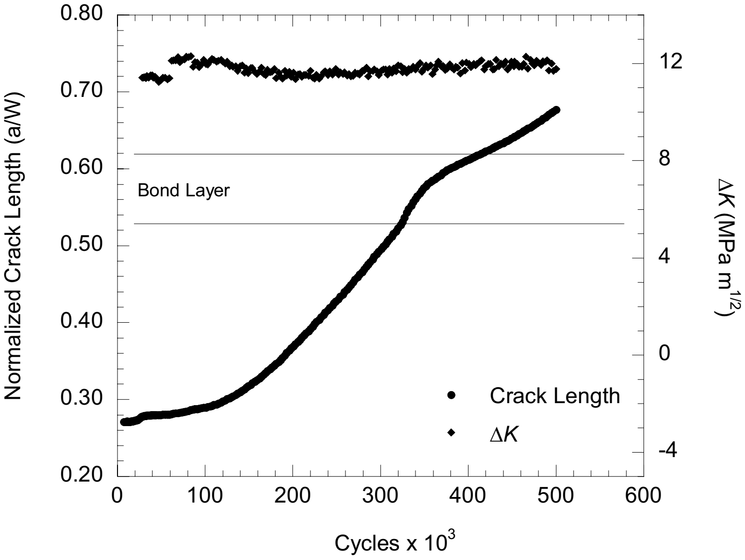

Figure 8. Normalized crack length versus cycles for test JNC-21: upper tube section, crack growing from outside to inside, nominal ΔK = 12 MPa√m.

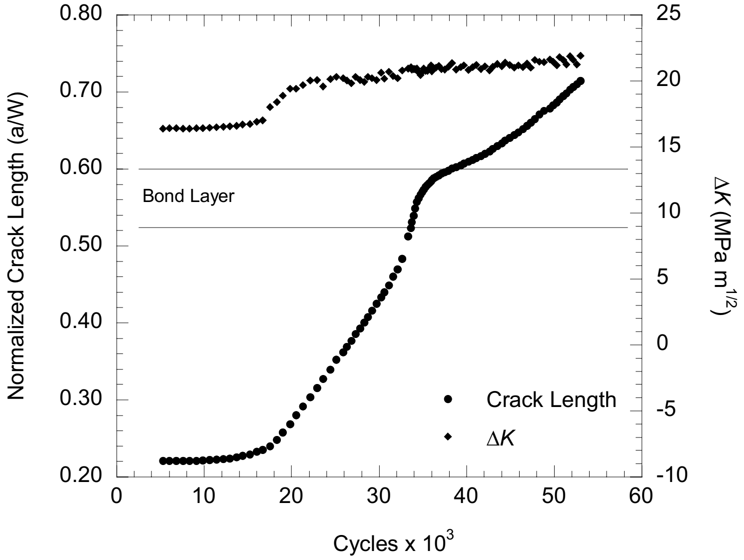

Figure 9. Normalized crack length versus cycles for test JNC-20: upper tube section, crack growing from outside to inside, nominal ΔK = 20 MPa√m.

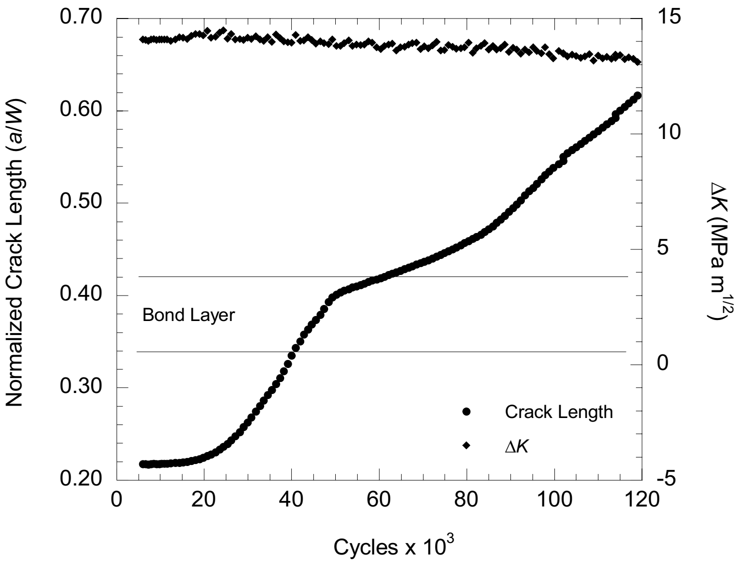

Figure 10. Normalized crack length versus cycles for test JNC-18, lower tube section, crack growing from inside to outside, nominal $\Delta K = 15$ MPa√m.

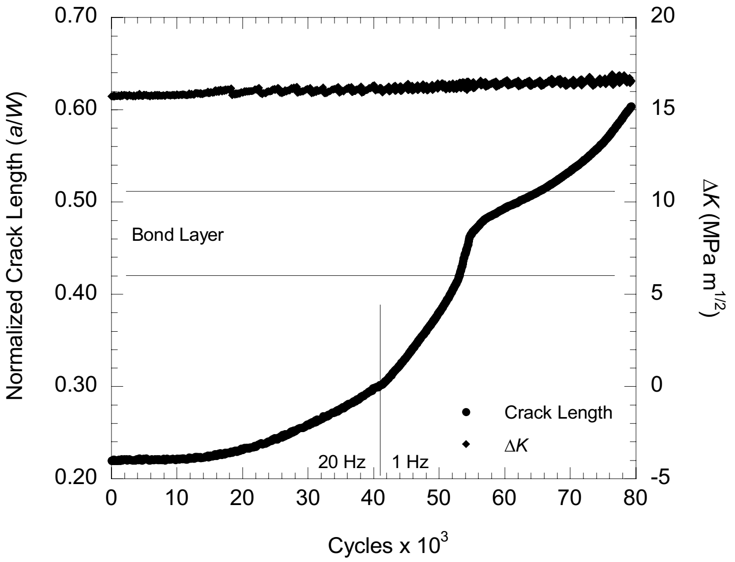

Figure 11. Normalized crack length versus cycles for test JAEA-400-10, upper tube section, crack growing from inside to outside, nominal $\Delta K = 16.5$ MPa√m, 400°C, humid Ar.

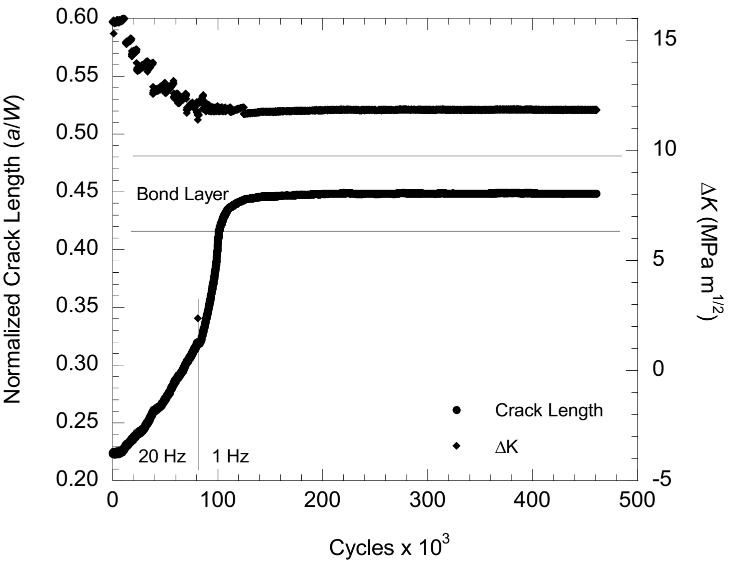

Figure 12: Normalized crack length versus cycles for test JAEA-400-6, upper tube section, crack growing from inside to outside, nominal ΔK = 12 MPa√m, 400°C, air.

3.3 Fractography

A light microscope overview of the fracture surface of a representative fatigue test specimen (JNC-22) is shown in Figure 13. All other specimens showed essentially identical features, regardless of ΔK level, crack growth direction, or location within the superheater. Tests performed at 400°C showed discoloration due to oxidation, but the fracture surface features were otherwise identical to the room-temperature features described below. The EDM notch is at the top and the fatigue crack growth area is in the center. The shiny bottom of the specimen is the area that was broken after cooling in liquid nitrogen. The metallurgical bond is clearly seen in the center of the fatigue area.

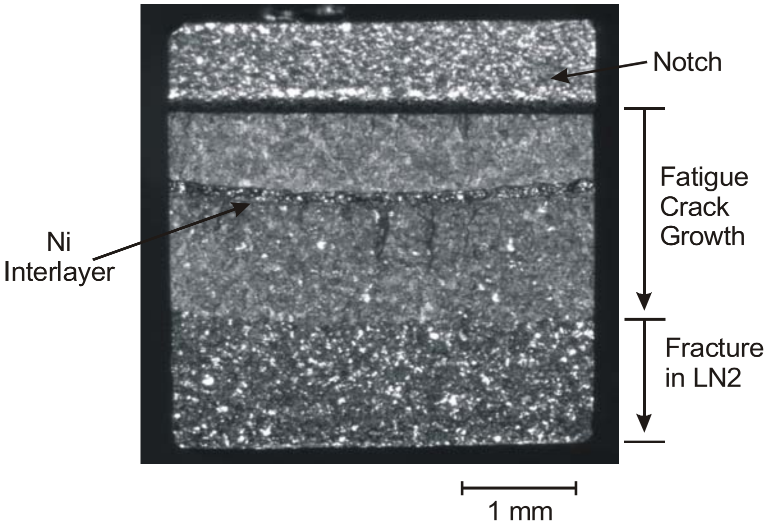

Figure 13. Overview of specimen JNC-22, upper tube section, crack growing from inside to outside, nominal ΔK = 15 MPa√m.

Figure 14 shows a closer view of the fatigue area taken in the SEM. The EDM notch is again at the very top of the image and the bond in the center. Note that the fatigue area after the bond layer is much rougher than before; the fatigue crack has apparently re-initiated on or been diverted to several levels after passing through the bond. The increased roughness is observed for a distance that corresponds with the area of reduced crack growth rate, as indicated on Figure 4. Similar features were observed on other specimens. Figure 15 shows typical fine-scale fatigue features prior to, immediately following, and well after the metallurgical bond. All areas show identical transgranular ductile rupture features, indicating no change in FCG mechanism in the base metal after passing through the bond layer.

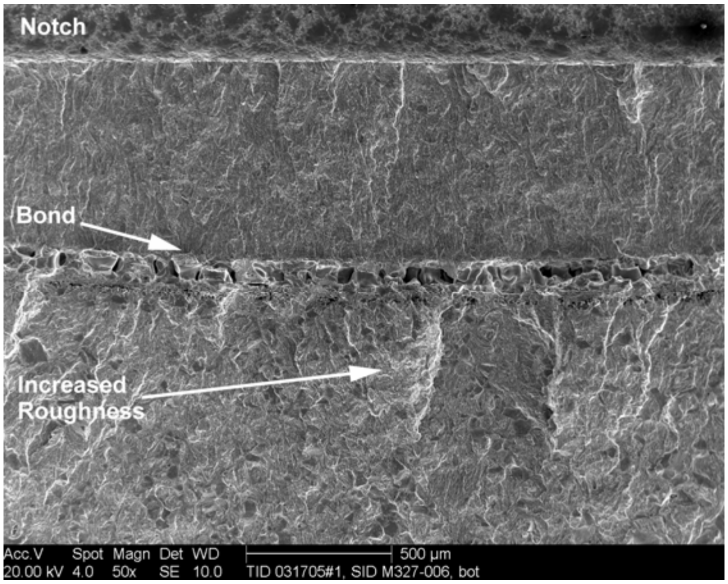

Figure 14. Overview of fatigue area in specimen JNC-22 (crack growth top to bottom).

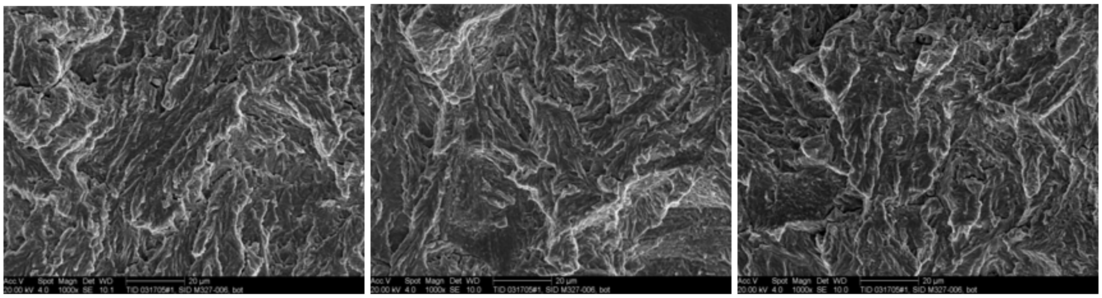
(a) (b) (c)

Figure 15. Typical fine-scale fatigue features (a) prior to the bond, (b) immediately after the bond, (c) well after the bond (specimen JNC-22, crack growth top to bottom).

Closer views of the features in the metallurgical bond are shown in Figures 16 and 17. Areas where the crack path has followed porosity are shown by smooth, featureless surfaces; other areas show faceted features with river markings indicating brittle facture or dimples indicative of ductile rupture. The cavernous nature of some areas of the bond porosity is apparent. Fine porosity on the outside tube side of the bond is also observed. A polished and etched (2% Nital) metallographic cross-section of the metallurgical bond, is shown in Figure 18 for comparison; similar porosity is present.

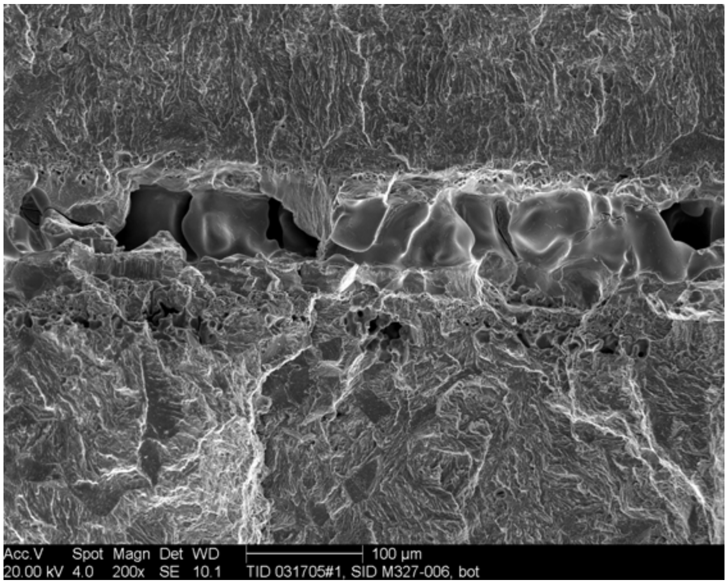

Figure 16: Fracture features in bond area (specimen JNC-22, crack growth from top to bottom).

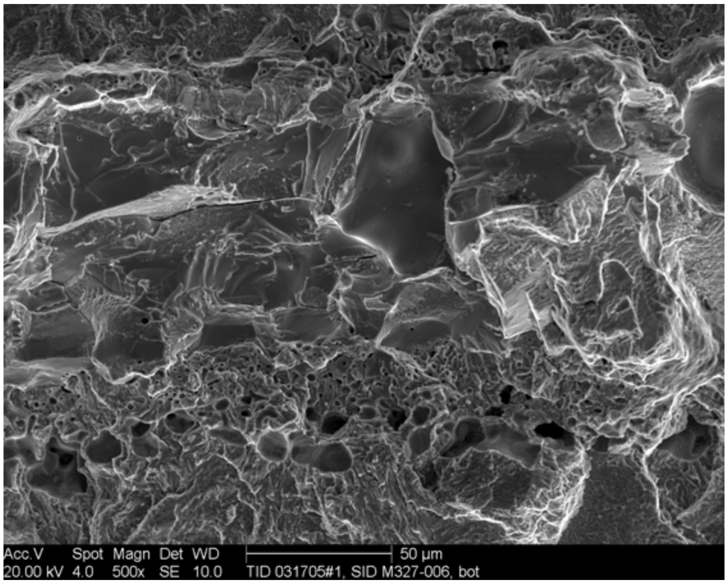

Figure 17: Fracture features in bond area (specimen JNC-22 crack growth from top to bottom).

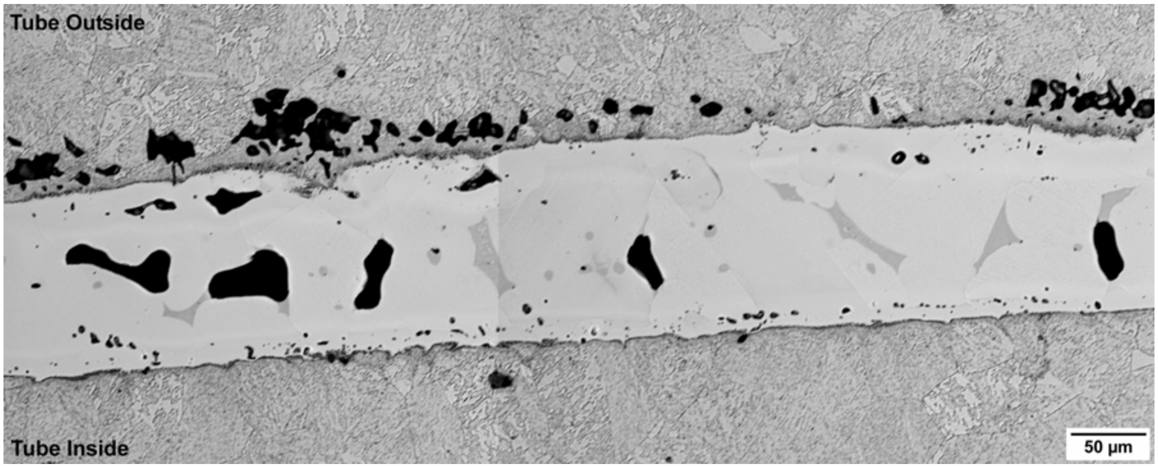

Figure 18: Polished and etched cross-section (normal to tube axis) of metallurgical bond in specimen JNC-22.

The metallographic cross-sections prepared from the JAEA-400-6 specimen confirmed that fatigue crack arrest occurred in the bond layer for this test performed at 400°C in air. Figure 19 shows a low-magnification overview of the crack. The starter notch is at the left and the crack propagates from the root of the notch and arrests at the far side of the bond layer, which is visible as the bright vertical band on the right side of the image. A higher magnification view of the crack tip (Figure 20) shows oxidation at the crack tip on the right side of the bond and at the bond interface on the left side. There is little oxidation associated with the crack in the bond layer itself, but the crack wake in the steel is clearly oxidized; therefore the bond layer appears more oxidation-resistant than the steel.

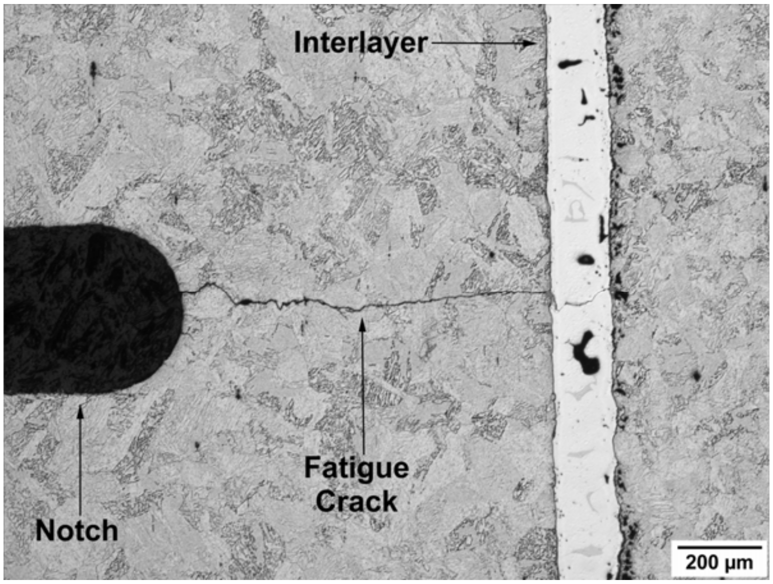

Figure 19. Low-magnification overview of JAEA-400-6 cross-section showing fatigue crack arrested at far side of interlayer.

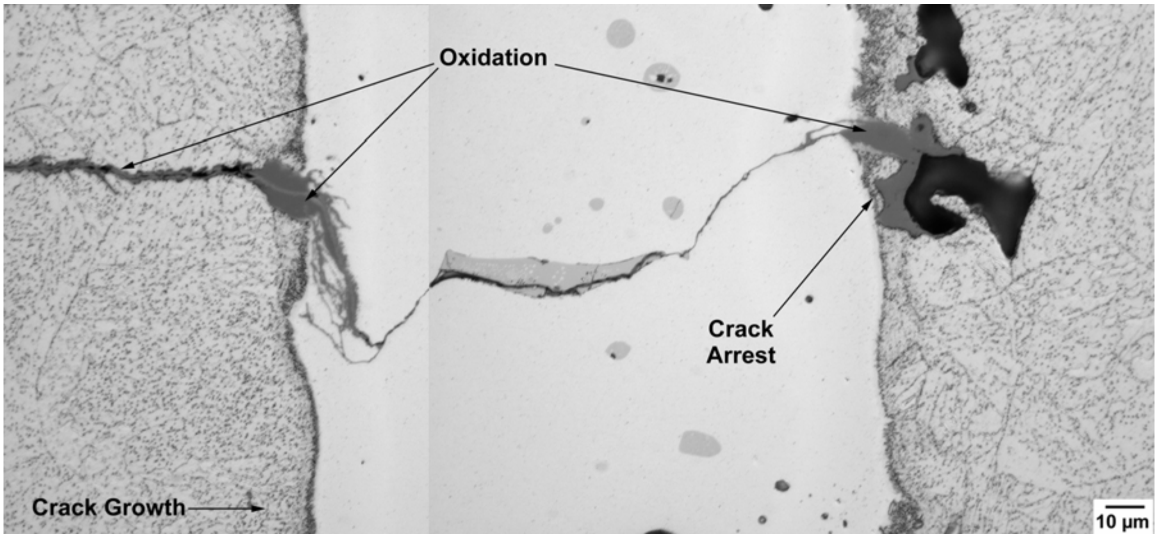

Figure 20: Close view of interlayer in Figure 19 showing oxidation at interlayer-steel interfaces and fatigue crack wake in steel.

4. Discussion

The results presented above indicate that at room temperature the presence of the metallurgical bond slows fatigue crack growth through the tube but does not result in complete crack arrest, at least for the ΔK levels tested. The effect of the bond appears to be independent of ΔK, location within the superheater (upper versus lower tube section), and crack growth direction (inside to outside versus outside to inside). Crack growth rates are accelerated in the bond, as expected given the high fraction of porosity in and near the bond. The retardation in crack growth rate after the bond appears to correlate with increased roughness of the fracture surface. The fact that crack growth is retarded for a significant distance after the bond indicates that retardation is not simply due to re-initiation of the crack on the opposite side of the bond; this is also supported by the absence of a true arrest of the crack at any point when passing through the bond layer.

Increased surface roughness is frequently associated with crack retardation due to closure effects, especially at the low R ratio used in the present tests (0.1). Increasing the R ratio, however, did not produce a significant change in the acceleration-retardation effect of the bond layer, contrary to the expectation if a significant closure effect were present. It is believed rather that the retardation results primarily from a disruption in the planarity of the fatigue crack as it passes through the highly porous bond layer. Although the crack does not have to re-initiate, it does appear to significantly deviate out of the original propagation plane in local areas when passing through the bond layer. Such disruption in crack uniformity reduces the effective ΔK at the crack tip and slows propagation. The local deviation of the crack path likely results from the connected, cavernous nature of the porosity in the bond layer. The crack will take the path of least resistance (highest porosity)—which involves growing out of the original crack plane in different areas along the crack width. After a period of growth in the base metal the crack again becomes uniform due to the uniformity of the far-field stress, and the growth rate returns to the baseline.

The retardation effect at room temperature, therefore, appears to be fundamentally related to the highly porous, cavernous nature of the interlayer. This retardation effect would likely not be present at the start of service when no porosity is present – the fatigue crack should readily grow through the atomistically-bonded interlayer, likely accelerated due to the softness of the pure Ni interlayer in comparison with the 2¼Cr–1Mo tube alloy.

Similar behavior was observed at 400°C, although a full crack arrest was observed for a low ΔK test in air. The crack arrest was likely assisted by oxidation of the base steel at the steel-bond interface, reducing ΔK by blunting the crack tip Oxidation-induced crack closure appears to have increased the threshold ΔK value from 9 to ~13 MPa√m for 400°C compared to room temperature. It is important to note that it is oxidation of the steel which appears to increase propensity for arrest, not oxidation of the interlayer itself. It is not surprising that the interlayer is more oxidation resistant than the base steel, since Ni is generally more oxidation resistant than Fe. It appears that the combination of reduced ΔK due to disrupted crack uniformity and blunting by crack-tip oxidation lead to arrest. The reduced frequency (1 Hz compared to 20 Hz) also plays a role by allowing more time for oxidation.

There was little difference in behavior between air and humid Ar at 400°C. Specimen surfaces were similarly oxidized after testing, with perhaps slightly less oxidation in humid Ar. Due to the simplicity of the test set-up, the humid Ar environment cannot be considered to be representative of a high-pressure steam system. Tests were performed in humid Ar as a simple check to see if the behavior might be markedly different than in air, which it was not. Proper confirmation of the behavior must be performed in an environment truly representative of the service environment, i.e. high-pressure steam. That said, however, it is appears likely that the behavior would not be very different than observed in the present tests, since oxidation of the steel or the Ni interlayer in steam will not be catastrophically severe, and their relative oxidation resistances will be similar.

Hence the function of the Ni interlayer as a fatigue crack arrestor appears to be limited. The interlayer retards crack growth over all ΔK values, but only results in crack arrest for near-threshold ΔK. Slower cycling frequencies and more oxidizing environments will increase the magnitude of ΔK at which arrest will occur. It worth repeating that the retardation function of the interlayer is only present because of the porosity defects caused by interdiffusion during service. A more effective interlayer for crack arrest would be one which did severely oxidize in the service environment.

5. Conclusions

Fatigue crack growth tests performed on specimens machined from metallurgically-bonded EBR-II superheater tubes show that the presence of the Ni bond layer results in a net retardation of growth as the crack passes through the layer both at room temperature and at 400°C. Even though growth rates in the layer itself are accelerated with respect to the 2¼Cr–1Mo steel tube material, crack growth in the tube material after passing through the bond layer is retarded by approximately a factor of two to three due to a reduction in crack front uniformity. The crack uniformity is disrupted by the presence of large, cavernous pores in the interlayer which locally deviate the crack out of the original crack plane by offering low-resistance crack paths. At 400°C in air blunting of the crack tip by steel oxidation at the steel-interlayer interface led to full crack arrest for a test conducted at a near-threshold ΔK level.

The effect of the interlayer appears to be independent of ΔK within the 12 to 20 MPa√m range tested, location within the superheater (upper versus lower tube section), and crack growth direction (inside to outside versus outside to inside). Baseline da/dN - ΔK curves obtained by similar tests on non-bonded superheater shell material agreed well with literature values for this alloy, indicating no effect of the extended thermal exposure on room temperature fatigue crack propagation resistance.

Table 1. Test conditions and results for room-temperature fatigue crack growth tests.

Test ID	Material	Crack Growth Direction	Nominal ΔK (MPa $m^{1/2}$)	Baseline rate prior to bond (mm/cycle)	Accelerated rate before/in bond (mm/cycle)	Retarded rate after bond (mm/cycle)	Re-accelerated rate after bond (mm/cycle)
JNC-03	Lower tube	Outside to Inside	15; actual 15-20.5	4.5×10^{-5} (15.8 MPa $m^{1/2}$)*	1.8×10^{-4} (17.8 MPa $m^{1/2}$)	1.9×10^{-5} (19.6 MPa $m^{1/2}$)	--
JNC-05	Shell	N/A	Varied	--	--	--	--
JNC-06	Shell	N/A	Varied	--	--	--	--
JNC-08	Shell	N/A	Varied	--	--	--	--
JNC-09	Shell	N/A	Varied	--	--	--	--
JNC-10	Shell	N/A	Varied	--	--	--	--
JNC-11	Lower tube	Outside to Inside	12; actual 11-14	8.7×10^{-6} (11.7 MPa $m^{1/2}$)	1.1×10^{-5} (11.8 MPa $m^{1/2}$)	8.7×10^{-7} (13.3 MPa $m^{1/2}$)	--
JNC-12	Lower tube	Outside to Inside	15; actual 14-21	3.9×10^{-5} (16.1 MPa $m^{1/2}$)	7.3×10^{-5} (18.5 MPa $m^{1/2}$)	2.3×10^{-5} (20.6 MPa $m^{1/2}$)	--
JNC-13	Lower tube	Outside to Inside	20	8.2×10^{-5}	4.4×10^{-4}	1.6×10^{-5}	--
JNC-14	Lower tube	Outside to Inside	10.5; actual 10.2-12	6.0×10^{-6} (10.5 MPa $m^{1/2}$)	1.1×10^{-5} (10.9 MPa $m^{1/2}$)	3.6×10^{-6} (11.6 MPa $m^{1/2}$)	5.8×10^{-6} (11.7 MPa $m^{1/2}$)
JNC-15	Shell	N/A	15	1.9×10^{-5}	--	--	--
JNC-16	Shell	N/A	12	6.7×10^{-6}	--	--	--
JNC-17	Lower tube	Outside to Inside	14	2.2×10^{-5}	3.3×10^{-5}	5.2×10^{-6}	--
JNC-18	Lower tube	Inside to Outside	14.5	2.3×10^{-5}	3.8×10^{-5}	6.7×10^{-6}	1.6×10^{-5}
JNC-19	Upper tube	Outside to Inside	14	2.3×10^{-5}	3.5×10^{-5}	7.0×10^{-6}	--
JNC-20	Upper tube	Outside to Inside	20	6.3×10^{-5}	2.2×10^{-4}	1.9×10^{-5}	3.8×10^{-5}
JNC-21	Upper tube	Outside to Inside	12	4.7×10^{-6}	8.2×10^{-6}	2.2×10^{-6}	--
JNC-22	Upper tube	Inside to Outside	14.5	2.2×10^{-5}	5.2×10^{-5}	8.9×10^{-6}	2.2×10^{-5}
JNC-23	Lower tube	Outside to Inside	14.7	2.5×10^{-5}	4.0×10^{-5}	--	--
JNC-24	Lower tube	Outside to Inside	12 ($R = 0.45$)	1.4×10^{-5}	3.1×10^{-5}	5.2×10^{-6}	--

*: Where actual ΔK values significantly deviate from nominal, the actual ΔK value is given below the rate.

Table 2: Test conditions and results for 400°C fatigue crack growth tests.

Test ID	Material, Environment	Crack Growth Direction	Nominal ΔK (MPa $m^{1/2}$)	Baseline rate prior to bond (mm/cycle)	Accelerated rate before/in bond (mm/cycle)	Retarded rate after bond (mm/cycle)	Re-accelerated rate after bond (mm/cycle)
JAEA-400-3	Shell, Air	N/A	Varied	--	--	--	--
JAEA-400-4	Upper tube, Air	Outside to Inside	14	$2.8x10^{-5}$	$5.2x10^{-5}$	$6.7x10^{-6}$	$1.6x10^{-5}$
JAEA-400-5	Lower tube, Airl	Inside to Outside	14.5	$2.0x10^{-5}$	$3.5x10^{-5}$	$7.7x10^{-7}$	--
JAEA-400-6	Upper tube, Air	Inside to Outside	12	$2.0x10^{-5}$	$5.4x10^{-5}$	Crack Arrest	--
JAEA-400-7	Upper tube, Air	Inside to Outside	19	$5.2x10^{-5}$	$1.4x10^{-4}$	$1.6x10^{-5}$	$4.5x10^{-5}$
JAEA-400-8	Shell Humid Ar	N/A	Varied	--	--	--	--
JAEA-400-9	Shell Humid Ar	N/A	Varied	--	--	--	--
JAEA-400-10	Upper tube, Humid Ar	Inside to Outside	16.5	$3.6x10^{-5}$	$1.1x10^{-4}$	$1.4x10^{-5}$	$3.8x10^{-5}$
JAEA-400-11	Upper tube, Humid Ar	Inside to Outside	14.5	$1.5x10^{-5}$	$4.3x10^{-5}$	$1.3x10^{-6}$	--